Mon. Not. R. Astron. Soc. **000**, 1–15 (2007) Printed 1 February 2008 (MN LATEX style file v2.2)

PKS1932-46: a radio source in an interacting group?⋆

K. J. Inskip[1]†, C. N. Tadhunter[1], D. Dicken[1], J. Holt[1], M. Villar-Martín[2], R. Morganti[3],
[1] *Department of Physics & Astronomy, University of Sheffield, Sheffield S3 7RH*
[2] *Instituto de Astrofísica de Andalucía (CSIC), Aptdo. 3004, 18080 Granada, Spain*
[3] *Netherlands Foundation for Research in Astronomy, Postbus 2, 7990 AA Dwingeloo, The Netherlands*

arXiv:0708.2848v1 [astro-ph] 21 Aug 2007

ABSTRACT

We present the results of a multiwavelength study of the $z = 0.23$ radio source PKS1932-46. Integral field unit spectroscopy using the Visible Multiobject Spectrograph (VIMOS) on the VLT is used to study the morphology, kinematics and ionisation state of the extended emission line region (EELR) surrounding this source, and also a companion galaxy at a similar redshift. Near- and far-infrared imaging observations obtained using the NTT and SPITZER are used to analyse the underlying galaxy morphologies and the nature of the AGN.

The host galaxy is identified as an $\sim$M$_\star$ elliptical. Combining Spitzer mid-IR with X-ray, optical and near-IR imaging observations of this source, we conclude that its AGN is underluminous for a radio source of this type, despite its status as a broad-line object. However, given its relatively large [OIII] luminosity it is likely that the AGN was substantially more luminous in the recent past ($\lesssim 10^4$ years ago).

The EELR is remarkably extensive and complex, reminiscent of the systems observed around sources at higher redshifts/radio powers, and the gas is predominantly ionised by a mixture of AGN photoionisation and emission from young stars. We confirm the presence of a series of star-forming knots extending north-south from the host galaxy, with more prodigious star formation occuring in the merging companion galaxy to the northeast, which has sufficient luminosity at mid– to far–IR wavelengths to be classified as a luminous infrared galaxy (LIRG).

The most plausible explanation of our observations is that PKS1932-46 is a member of an interacting galaxy group, and that the impressive EELR is populated by star-forming, tidal debris. We suggest that the AGN itself may currently be fuelled by material associated either with the current interaction, or with a previous merger event. Surprisingly, it is the companion object, rather than the radio source host galaxy, which is undergoing the bulk of the star formation activity within the group.

Key words: galaxies: active – galaxies: evolution – galaxies: ISM – galaxies: haloes – galaxies: interactions – galaxies: individual: PKS1932-464

1 INTRODUCTION

Extended emission line regions (EELRs) are often observed around powerful distant radio sources (McCarthy et al 1987), and their observed properties (size, luminosity, kinematics and ionisation state) are known to depend strongly on those of the radio source (e.g. Best et al 2000, Inskip et al 2002a, Moy & Rocca-Volmerange 2002). Although the behaviour of the emitting material and the balance between different ionisation mechanisms is now becoming increasingly well understood, many outstanding questions still remain. The origin of the extended emission line gas is one such issue. Does it exist *in situ* prior to the onset of the radio source? Is it formed from material driven out of the host galaxy by AGN/radio source/starburst related outflows? Is it infalling material associated with a cooling flow? Or, is it produced via galaxy interactions/mergers associated with the radio source triggering event? A secondary issue is whether the distribution of material is related to its origin, and its eventual fate. As the properties of this gas may have close links with both the origin of radio source activity and the host galaxy evolution, these are particularly pertinent questions.

While the emitting material is most frequently observed

⋆ Based on observations collected at the European Southern Observatory, Chile (program 075.B-0820(A) and 078.B-0500(A)).
† E-mail: k.inskip@shef.ac.uk

either along the radio source axis or within AGN ionisation cones, recent observations have shown that this is not always the case. Extensive emission line regions lying almost perpendicular to the radio axis have been identified around several radio sources, via recent narrow band imaging observations (Tadhunter et al 2000, Solórzano-Iñarrea et al 2002, Villar-Martín et al 2005). These features may perhaps be related to the large gaseous haloes observed at higher redshifts (e.g. Röttgering et al 1995, van Ojik et al 1997, Jarvis et al 2003, Villar-Martín et al 2003), but their exact nature is still an open question. Large, complex EELRs with no clear-cut link with the radio source morphology have also been observed around low redshift quasars, e.g. 4C 37.43 (Fu and Stockton 2007, Stockton et al 2002).

The EELR surrounding the FRII radio galaxy PKS1932-464 ($z \sim 0.231$) is a prime example of such highly complex systems. Previous imaging and spectroscopic observations of this source (Villar-Martín et al 1998, Villar-Martín et al 2005; hereafter VM98 and VM05) have shown that the host galaxy is surrounded by an extensive ($\sim$ 100kpc radius), knotty emission line region, extending well beyond the observed radio source. As well as material lying along the radio source axis, emission is also observed from structures lying at large angles to the radio source axis, which are unlikely to lie within the AGN ionisation cone. VLT long-slit spectroscopy at position angle PA -9, misaligned by 63° from the radio source axis (PA -72), has determined that this off-axis emission is likely to be due to star-forming objects (VM05).

Extreme EELR features such as those displayed in the case of PKS1932-464 (extreme size, chaotic morphology of the ionised gas, off-axis star-forming knots and radio source asymmetries) are generally more common at higher redshifts than they are at lower redshifts (particularly in terms of EELR morphologies and kinematics; Inskip et al 2002b). Similar trends with redshift are observed for the continuum emission from these regions (the *Alignment effect*; Chambers, Miley & van Breugel 1987; McCarthy et al. 1987; Allen et al 2002). In part, these trends are due to an increased incidence of jet-cloud interactions at higher redshifts, but environmental factors may also play an important role. At lower redshifts the general trend is for smaller, more regular EELRs which are usually (but not always) well-aligned with the radio source axis. Previous spectroscopy of PKS1932-464 has not isolated the extreme kinematics typical of jet-cloud interactions, and the complex distribution of star-forming EELR material (a rarity at such low redshifts) and the proximity of a possible companion galaxy are suggestive that galaxy interactions and environmental factors are the primary cause of the observed EELR features.

One option for exploring these systems in detail is the use of integral field spectroscopy (IFS). IFS studies of EELRs have the potential to greatly improve our understanding of these systems, particularly in terms of building up a consistent explanation for the nature, distribution and origin of the emission line gas, and the links with the radio source triggering mechanism. The additional spatial data provided by IFS observations is a major advantage, as it allows the EELR properties (physical conditions, gas dynamics, ionisation state) to be efficiently studied and quantified as a function of position relative to the radio source, rather than just along the radio axis. Most previous long slit studies have concentrated on the radio axis position angle, and are therefore biased towards the regions for which the gas kinematics are perturbed by the growing radio source rather than reflecting the intrinsic properties of the extended halo.

In this paper, we present the results of a multi-wavelength study of PKS1932-464, combining optical IFS spectroscopy with near and far infrared imaging observations, and allowing us to greatly expand on the previous work carried out on this source (VM98, VM05). The details of the source, our observations and data reduction are described in section 2, and the results presented in section 3, including an analysis of the properties of the galaxy previously assumed to be a nearby companion. In section 4, we discuss the implications of our results, and we present our conclusions in section 5. Throughout this paper, we assume cosmological parameters of $\Omega_0 = 0.3$, $\Omega_\Lambda = 0.7$ and $H_0 = 70 \mathrm{km\,s^{-1}\,Mpc^{-1}}$, which result in an angular scale of 3.7kpc/arcsec at $z = 0.23$.

2 SOURCE DETAILS, OBSERVATIONS AND DATA REDUCTION

2.1 PKS1932-46

As described in the introduction, the EELR surrounding PKS1932-46 is quite remarkable for a low redshift radio galaxy. However, this paper also considers the wider properties of the host galaxy and radio source in addition to the EELR, and it is therefore appropriate to briefly outline the other key properties of this source.

PKS1932-46 is an FRII radio galaxy lying at a redshift of $z \sim 0.231$ with a total radio power of $5.5 \times 10^{26} \mathrm{WHz^{-1}}$ at $\sim$ 5GHz (Morganti, Killeen & Tadhunter 1993). Its radio structure (VM98; see also Fig 1) is somewhat asymmetric; the western radio lobe has a projected physical extent of 41kpc cf. 26kpc for the eastern radio lobe. Core emission is observed weakly at 2.3 and 8.6GHz (Morganti et al 1997; VM98), and the source has an R-parameter of $R_{2.3\mathrm{GHz}} = 0.0023$. In terms of polarisation, the western lobe appears more strongly polarised than the eastern lobe, with strong depolarisation of the eastern lobe at lower radio frequencies (VM98), possibly due to warm emission line gas in this region.

2.2 VIMOS IFU spectroscopy

Integral field unit (IFU) spectroscopic observations were carried out using the Visible Multiobject Spectrograph (VIMOS; Le Févre et al 2003, Scodeggio et al 2005), on 2005 June 4, 2005 June 7, and 2005 June 8, as part of the European Southern Observatory (ESO) observing programme 075.B-0820(A). VIMOS is mounted on the Nasmyth focus of the UT3 Melipal unit of the Very Large Telescope (VLT). Our data were obtained using the medium resolution (MR-orange) grism and the GG475 order sorting filter; in this configuration, the IFU consists of 1600 microlenses coupled to 0.67-arcsec diameter fibres, covering a total sky area of 27×27 arcsec^2, with a useful wavelength range of $\sim 4500 - 9000$Å. The instrumental spectral resolution, as determined from unblended skylines, was approximately 7Å

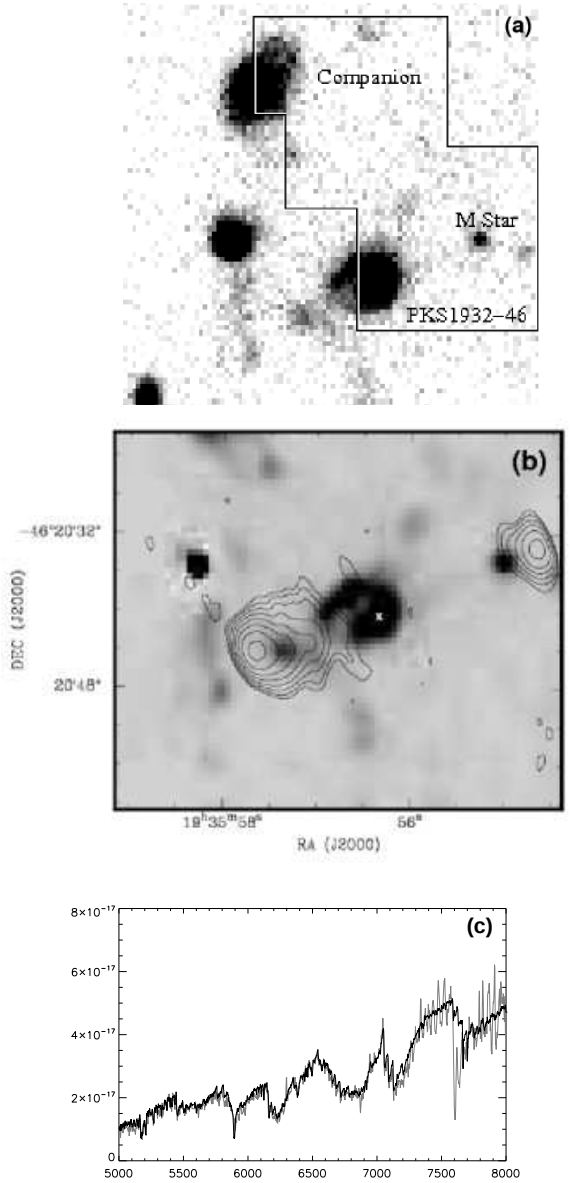

Figure 1. (a - top) [OII]+continuum image of PKS1932-46 and the surrounding field (from VM98), illustrating the approximate IFU field of view and identifying individual objects. (b - centre) 5.8 GHz radio contours overlaid on an [OII]+continuum image (from VM98), illustrating the relative size of the radio source. (c - bottom) Extracted spectrum of the M star lying to the west of PKS1932-464 (dashed line), overlaid with a linearly scaled 50% mixture of M2 and M3 SDSS stellar cross-correlation template spectra (solid line).

(FWHM). The total integration time was $\sim$ 12450s; full details of the observations and observing conditions are given in Table 1. The data were obtained with two separate pointings, giving an overall field of view with a maximum extent of 41 arcseconds. As well as allowing a larger region of the EELR and additional objects to be studied, large offsets between exposures should ideally have facilitated accurate sky subtraction.

Data reduction was carried out using the VIMOS Interactive Pipeline and Graphical Interface (VIPGI) software package (Scodeggio et al 2005, Zanichelli et al 2005); here we summarise the basic steps involved, which include some variations from the standard VIPGI procedures. In the first stage of the reduction process, bias subtraction and flat fielding is carried out separately for the four IFU quadrants. For each target/spectrophotometric standard star observation, the locations of the spectra for each individual fibre are identified and traced using continuum lamp exposures. Once all spectra locations have been accurately traced, the spectra are wavelength calibrated using arc-lamp observations obtained using the same instrumental set-up, with resulting residuals typically ~ 0.3Å per fibre on average. The third stage of the reduction process is the extraction of individual spectra. Each individual fibre spectrum is extracted in two dimensions, converted to a linear wavelength scale, and summed spatially to form a one-dimensional spectrum. Cross-talk effects due to fibre–to–fibre contamination are likely to be minimal (uncertainties of the order of $\sim 5\%$); as any corrections would introduce uncertainties of a similar magnitude (Zanichelli et al 2005), no corrections are made for this effect. Cosmic rays were detected and removed from the data using a 6σ clipping algorithm evaluated within a 40 pixel box. The instrumental sensitivity function for each IFU quadrant was determined using the summed extracted spectra of spectrophotometric standard star frames; this is then applied to the science frames to produce spectra with accurate relative flux calibration. The data from 2005 June 7 and 2005 June 8 were obtained in non-photometric conditions, and were flux calibrated via reference to the photometric data obtained on 2005 June 4.

Table 1. Details of the VIMOS and SOFI observations and observing conditions. The seeing measurements are given for the wavelength of the observations.

Date	Instrument	Exposure time (s)	Seeing	Photometric?
20050604	VIMOS	4980	0.3-0.7″	Fully
20050607	VIMOS	4980	0.8-1.2″	Partially
20050608	VIMOS	2490	0.6-0.7″	Partially
20061114	SOFI	3000	0.8″	Fully

Analysis of the night sky emission lines was used to correct for variations in fibre-to-fibre transmission. At this stage we also used the locations of six bright unblended skylines to manually apply a corrective linear shift in wavelength for each observation, for the minority of fibres affected by this common fault. An average sky spectrum can also be produced and subtracted from the data. However, for observations of targets with extensive emission line regions, this step has an unfortunate tendency to oversubtract flux in the vicinity of bright emission lines, even when the majority of the field of view covers blank sky. Pipeline sky subtraction was therefore not applied to our data. At this stage, we instead created three different versions of each observed frame. In the first version, we treat each frame as if it were long-slit data: the fibres which include emission from our target and other objects are identified (using the final data cube; by necessity, this process is iterative in nature) and masked, and the remaining fibres were used to derive a sky spectrum which is subtracted from the data. This is effectively the same method as that used by the pipeline for sky subtraction, but with the advantage that the relative flux levels of emission line regions are not corrupted. For our second data set, we subtracted from each frame the data

taken with the alternative pointing position obtained immediately before/after the frame in question. This removes the sky flux and also gives an accurate fringing correction, but where emission from different objects lies at the same fibre position in both pointings, object flux subtraction also occurs. However, comparison with our other data sets allows the affected fibres to be very clearly identified. Finally, we also retained an unaltered data set which included the full sky emission, in order to have a means of identifying any spurious features introduced by our treatment of the previous data sets.

The final stage of the reduction process was the creation of a datacube, combining the four quadrant frames together and median averaging each observation. As our data were obtained over several nights (with different calibration data and observing conditions for each), we initially kept the data for different nights and the two pointing positions separate. Fringe correction is an optional part of this process, but was not included in our reduction as it cannot accurately distinguish between the excess flux of fringing and spatially extended line emission. Although the VIMOS pointing is accurate within a given set of observing blocks, this accuracy is not maintained between observations made on different nights. The creation of our final data cubes included one last step: registration and shifting of the individual cubes based on the position of bright point sources in the IFU field of view.

Fig. 1 displays two [OII]3727Å+continuum images of the field of PKS1932-46 (from VM98), the first illustrating the field of view of our IFU data, and the second showing the relative extent of the radio emission. Our data, obtained with two separate pointings, include the host galaxy, the EELR to the west, and the companion object to the northeast. The somewhat unusual shape of our final FOV is caused by a block of faulty fibres within the southeast quadrant of the IFU. Extracted IFU spectra confirm that the galaxy to the north-east lies at a redshift of $z = 0.2298 \pm 0.0002$, similar to that of the radio source itself ($z = 0.2307 \pm 0.0002$). The bright object lying within the western radio lobe is an M2/3 star; in Fig. 1 we also display a comparison between M2/M3 SDSS stellar cross-correlation template spectra (Stoughton et al 2002) and our extracted spectrum for this object, confirming its nature as a foreground star.

2.3 SOFI Ks-band imaging

Ks-band imaging observations of PKS1932-46 were obtained on 2006 November 14 (see Table 1 for details). Fifty 1-min exposures were obtained using the SOFI instrument (Moorwood, Cuby & Lidman 1998) on the ESO 3.5-m New Technology Telescope (NTT). The instrument was used in the small field mode, giving a plate scale of 0.144 arcsec per pixel, and each observation was subject to a random offset within a 40 arcsec diameter box, resulting in a typical field of view of $\sim 3 \times 3$ arcmin. The data were corrected for SOFI's interquadrant row cross talk effect using an adapted version of the SOFI crosstalk.cl IRAF script. The data were flat-fielded using the following process: all target frames were combined, median filtered and normalised to a mean pixel value of 1.0 to create a first-pass flat-field image, which was then applied to each frame. Bright objects on the flat-fielded images were then masked out, and the process repeated with the masked frames, allowing the data to be cleanly flat fielded without any contamination from stars or galaxies. The flat-fielded data were sky-subtracted and combined using the IRAF package DIMSUM, creating a final mosaiced image of approximately 180×180 arcsec^2, which was flux calibrated using observations of NICMOS Photometric Standard stars (Persson et al 1998), giving a photometric zero-point magnitude of $K_S = 22.347 \pm 0.010$. The data were corrected for galactic extinction using $E(B-V)$ values for the Milky Way from the NASA Extragalactic Database (Schlegel et al 1998), and the parametrized galactic extinction law of Howarth (1983).

Table 2. Details of our Spitzer MIPS and SOFI K_S-band photometry of PKS1932-46 and the surrounding field. Columns 1 and 2 list the wavebands and total exposure times. Columns 3 and 4 give the extracted fluxes of PKS1932-46 and the nearby spiral companion galaxy. The K_S-band fluxes were evaluated within circular apertures with 5 and 12 arcsecond radii, and the MIPS data are total object fluxes derived from measurements of the PSF over various apertures (typically 3-20 arcsecond radii). The 160μm flux of PKS1932-46 is a 3-sigma upper limit.

Waveband	Exposure time (s)	Observed Flux (mJy) PKS1932-46	Companion
2.16μm (5″)	3000.0s	0.60±0.02	1.38±0.03
2.16μm (12″)	3000.0s	0.64±0.02	1.61±0.03
24μm	180.4s	2.5±0.1	4.4±0.4
70μm	545.3s	17.6±2.4	48.3±5.1
160μm	167.8s	< 94.4	198.1±31.5

2.4 Spitzer MIPS photometry

Spitzer MIPS (Werner et al 2004; Rieke et al 2004) photometry of PKS1932-46 was carried out as part of a program of observations of a large sample of 2Jy radio galaxies (see Tadhunter et al 1993 for sample definition). The Spitzer observations were made on 2006 May 5 in each of the 24μm, 70μm and 160μm wavebands; details of the observations are provided in Table 2. The data were reduced using the MIPS pipeline (Gordon et al 2005, Masci et al 2005) and the MOPEX mosaicing software (Makovoz & Khan 2005, Makovoz & Marleau 2005) provided by the Spitzer Science Center. In addition to the standard mosaicing procedure, we have also used a column filtering process on the 70um data (obtained from the Spitzer Science Center's contributed software resource), and an overlap correction program on the the 24μm data (available on the Spitzer Science Center website).

3 RESULTS

3.1 The host galaxy

Figure 2 displays our new $Ks-$band imaging observations of PKS1932-46 and its surrounding field. The radio source host galaxy lies towards the bottom of the field, and is a fairly regular elliptical. It has a total K_S-band magnitude (Galactic extinction corrected and evaluated within a 10 arcsecond/37 kpc diameter aperture) of 15.11 ± 0.03. The two sources at declinations $\sim -46°20'36''$ are both point sources; the western object (R.A. $\sim 19^h35^m55^s.2$) is known to be an

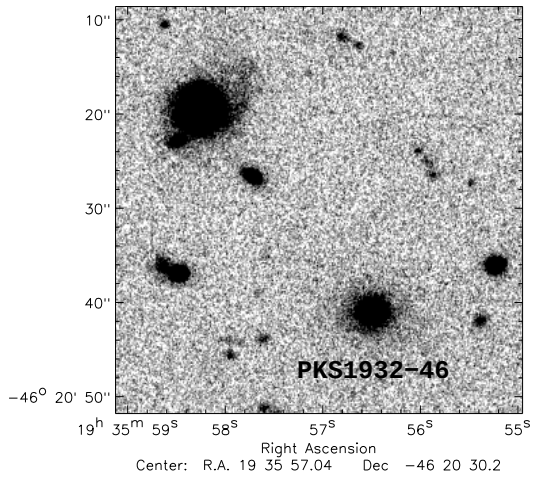

Figure 2. SOFI $Ks-$band image of PKS1932-464 (lower right, labelled) and the surrounding field.

M2/M3 star, while the eastern object (R.A. $\sim 19^h35^m58^s.6$) lies adjacent to some more diffuse emission to the east. The large object to the north-east of the field with a similar redshift to PKS1932-46 is a disturbed galaxy with clear signs of a double nucleus and a tidal tail; this object has a 10 arcsecond diameter aperture magnitude of 14.21 ± 0.02 in the K_S-band, and will be discussed in greater depth in section 3.3.

We have modelled the host galaxy morphology within a 32×32 arcsec^2 region using the methods detailed in Inskip et al. (2005), which can be briefly summarised as follows. The point spread function (PSF) for the SOFI field can be accurately determined from unsaturated stars within the mosaic field; their 2-d profile is extracted, normalised to unit flux, and used to generate an average PSF profile. In order to avoid any complications arising from variations in image quality across the SOFI field of view, we use the nearby M2 star lying to the west of the galaxy. Comparison with other stars in the field confirms that the image quality is generally good, and that this star does not suffer noticeably from contamination by any nearby faint objects. Once a good PSF had been obtained, de Vaucouleurs profile galaxy models were convolved with the PSF and fitted to the surface profile of the galaxy, using available least squares minimisation IDL routines[1]. The free parameters for this modelling are the galaxy flux, centroid, effective radius, and fractional nuclear point source contribution. Galaxy ellipticity was also allowed to vary, but in the case of this object did not lead to significant variation in the preferred effective radius, nuclear point source contribution, or distribution of residual flux.

The modelled data and model-subtracted residuals are displayed in Fig. 3, together with a plot of the variation in reduced χ^2 over the parameter space considered. The resulting best-fit parameters give an effective radius of $r_{\rm eff} = 2.49 \pm 0.66$ arcsec (equivalent to 9.18 ± 2.43kpc in our assumed cosmological model), and an unresolved nuclear point source contribution of $15.9 \pm 2.2\%$. The residuals (which remain present at a low level regardless of the model ellipticity) display some level of asymmetry, with the model slightly underfitting the galaxy westwards of the nucleus and overfitting it immediately north and south of the nucleus (see Fig. 3(b)). These residuals are likely to reflect the intrinsic asymmetries of the source (as noted in VM98; e.g. the "arm" structure extending eastwards and the N-S aligned star-forming knots). Possible causes are contamination of the galaxy emission by asymmetrically distributed young stellar populations (which although blue in colour would still be expected to boost the observed-frame $K-$band flux; see e.g. Inskip et al 2006), or alternatively, the presence of a dust lane lying perpendicular to the radio source axis. We also extended our modelling to Sérsic profiles (Sérsic 1968; i.e. $r^{1/n}$ rather than simply $r^{1/4}$), so as to investigate alternative galaxy profiles. The range of acceptable Sérsic indices for our modelling is $n = 2.75 \pm 1.41$, with other parameters of $r_{\rm eff} = 5.44 \pm 4.05$ and a point source contribution of $19\pm5\%$. These relatively large error bars reflect the fact that there is clearly some level of degeneracy within the models, and disky elliptical profiles can provide reasonably good fits to the observed data with similar residuals to the de Vaucouleurs profile models.

PKS1932-464 was one of twelve radio galaxies to be studied by Holt et al (2007), in their detailed modelling of the continuum properties and stellar populations of the host galaxies. The galaxy spectrum is best fit by a combination of a power law and an old stellar population (aged ~ 12.5 Gyr); although the addition of a young stellar population component can also result in good fits to the data, the subsequent degeneracy between the power law shape and YSP mass/age cannot be resolved. Taking their assumed old stellar population and convolving a GISSEL spectral synthesis (Bruzual & Charlot 2003) template spectrum with the K_S band filter profile implies that a galaxy of this age and magnitude ($K_S = 15.3$, after removal of point source component; this is close to the $L\star \sim 15.5$ magnitude expected at this redshift (e.g. Kochanek et al 2001, Willott et al 2003)) would have a mass of approximately $2.8\times10^{11}M_\odot$. More luminous, younger stellar populations would of course require less mass; varying the galaxy age from 5 to 15 Gyr allows for a mass range of $1.7 - 3.2 \times 10^{11}M_\odot$.

3.2 EELR properties

The EELR lying in and around the western radio lobe of PKS1932-46 is very complex, and our data reveal a number of feaures that have not been previously identified. In the following sections we will discuss the morphology, kinematics and ionisation state of the EELR in turn, making full use of the versatilty of our IFS data, which is presented in several different ways in order to best illustrate the different EELR features.

Figures 4 and 5 concentrate on a small region of the IFS datacube which covers the host galaxy and western radio lobe. Fig. 4 displays a continuum image of the field and the continuum-subtracted summed [OIII]5007Å emission line image, while Fig. 5 displays the continuum-subtracted flux stepped in equal ~ 2.5Å spectral bins (equivalent to $\sim$110km s^{-1}) over the wavelength range 6146-6174Å (i.e. covering the [OIII]5007Å emission line). This approach allows the continuum and line emitting regions to be con-

[1] MP2DFUNFIT.PRO, part of Craig Markwardt's MPFIT nonlinear least squares curve fitting package available via http://astrog.physics.wisc.edu/∼craigm/idl/fitting.html.

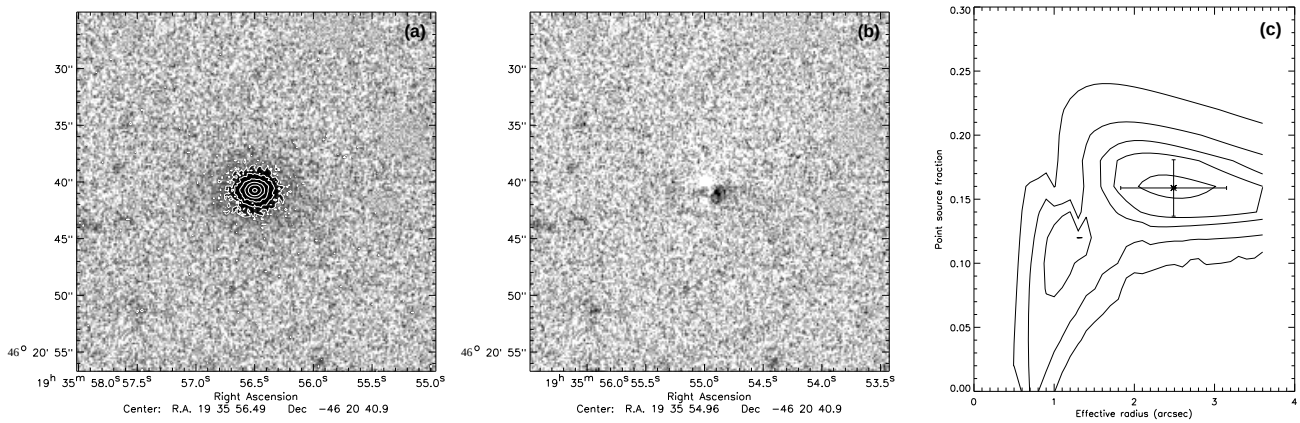

Figure 3. Host galaxy morphology fits for PKS1932-46. The $K-$band galaxy image is presented in frame (a), with the residuals after best-fit model galaxy subtraction displayed in frame (b). Frame (c) illustrates the 1, 2, 3, 5 and 10-σ contours for the reduced χ^2, plus the best-fit values and associated error bars for the point source contribution and effective radius.

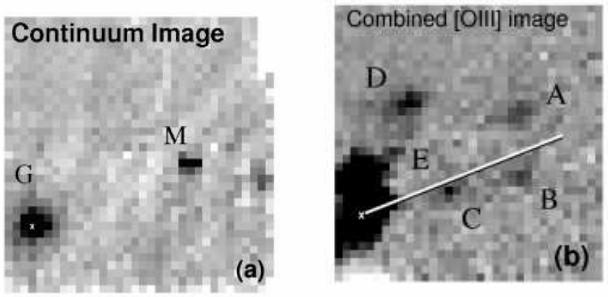

Figure 4. (a – left) Continuum image of PKS1932-46 generated from the emission either side of the [OIII]5007Å emission line. The host galaxy and nearby M-star are labeled with the letters G and M respectively. (b – right) Continuum-subtracted [OIII]5007Å emission line image generated from summed data between ∼6146Å and ∼6174Å. Noteworthy emission line features are labelled A-E. In these figures, north is to the top and east to the left, the pixel scale is 0.67″/pixel (giving a total field of view of $\sim 23.5 \times 23.5$ square arcsec or 87×87kpc^2), and the radio source axis (marked with a line illustrating the approximate extent of the western lobe) lies at a position angle of $-72°$. The position of the host galaxy centroid is marked in both frames with a cross.

sidered separately, and provides a clear image of the varied velocities of the line-emitting material.

In order to study the EELR properties in greater detail, we have developed IDL routines to model the line emission on a fibre-by-fibre basis. For each fibre spectrum, we locate a selected emission line and fit it with one or more Gaussian components plus a continuum, extracting the resulting modelled emission-line flux, FWHM and velocity offset relative to the systemic redshift of PKS1932-46. The resulting data are displayed in Fig. 6, and provide a more global overview of the kinematics of the system. Fig. 6 also includes data from the companion galaxy lying to the northeast of PKS1932-46.

3.2.1 EELR morphology

As Fig. 4 and Fig. 6 illustrate, the EELR surrounding PKS1932-46 extends throughout the western radio lobe, and contains a number of discrete, spatially resolved features in addition to the powerful line emission centred on the host

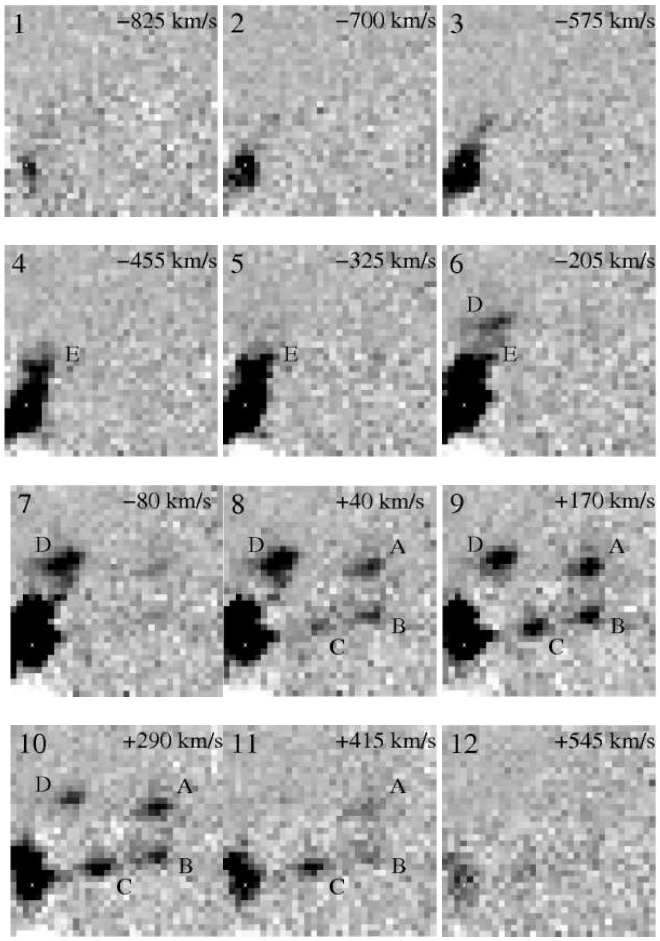

Figure 5. IFU flux images of PKS1932-46 and the western EELR generated from consecutive ∼2.5Å spectral bins, from ∼6146Å (top left) to ∼6174Å (bottom right). These wavelengths correspond to 4993–5015Å in the rest-frame of PKS1932-46 (i.e. $z \sim 0.231$), and cover the [OIII]5007Å line emission. Labelling of different features is the same as that used in Fig. 4, and we also denote the velocity offset of each frame relative to the typical redshift of $z = 0.231$. The position of the host galaxy centroid is marked in all frames with a cross.

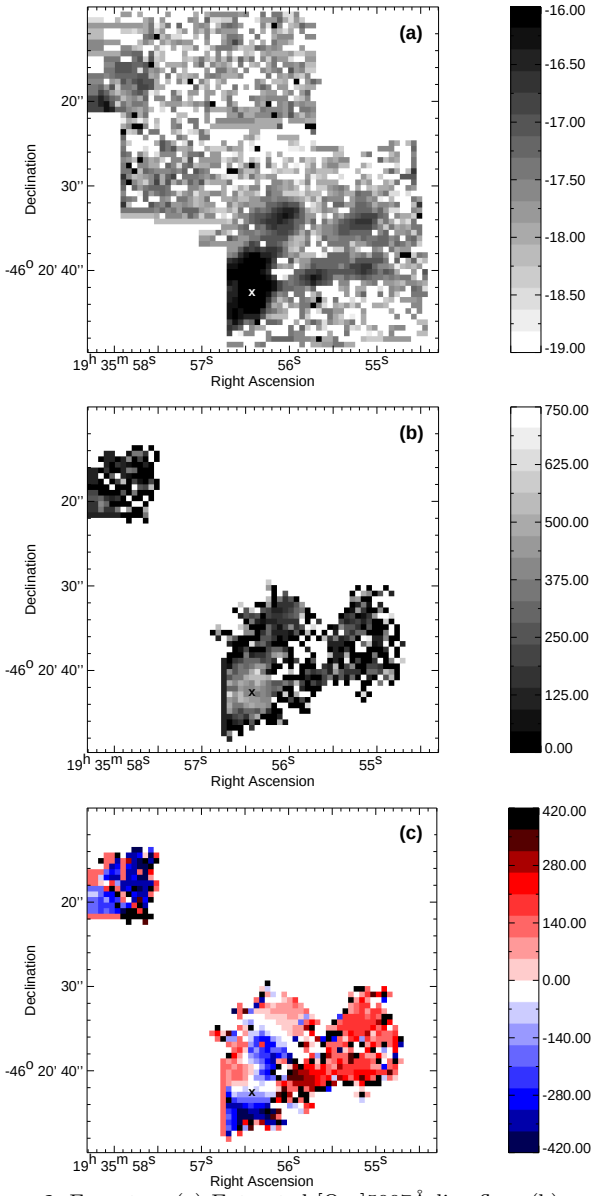

Figure 6. From top: (a) Extracted [OIII]5007Å line flux; (b) extracted [OIII]5007Å FWHM line width (corrected for instrumental broadening); (c) velocity shift of [OIII]5007Å relative to $z = 0.231$ (the approximate rest frame of the host galaxy). The position of the host galaxy centroid is marked in all frames with a cross. The grey-scale bars illustrate either log(flux) in units of $\mathrm{erg\,s^{-1}cm^{-2}}$ or velocities in $\mathrm{km\,s^{-1}}$. For the plots of FWHM and velocity offset, we have masked the fibres with an [OIII] emission line flux below $1 \times 10^{-18}\mathrm{erg\,s^{-1}cm^{-2}}$.

galaxy itself. However, the full complexity of the EELR is only revealed once we can disentangle the different velocity components in the emitting material. Figure 5 illustrates twelve consecutive continuum-subtracted slices of the IFS datacube covering the [OIII]5007Å emission line. The western radio lobe contains a series of resolved clumpy features (labelled A-C in Figs. 4b and 5) which produce [OIII]5007Å emission at the longest wavelengths. While we cannot pin down precise locations of the emission features relative to the radio source cocoon along the line of sight, the observed features in the western lobe all have very similar redshifts, and lie at a variety of distances between the host galaxy and the radio hotspot.

The bright knots to the north of the host galaxy (labelled D & E in Figs. 4 and 5) lie at a considerable angular distance from the radio source axis: knot D lies $\sim 10''/35$kpc away from the AGN along a PA of $\sim -30°$, and has been detected in previous emission line imaging (VM98). As Fig. 5 illustrates, it can be immediately discerned that these knots lie at different redshifts to the other EELR knots in the western lobe, and that there appears to be a velocity gradient between knots D and E.

The central regions of the EELR display the most intense line emission, at several different velocities. In addition to the "arm" structrure (Fig. 5 frame 10) lying to the east of the host galaxy which was noted in previous observations (VM98), we also observe blue-shifted emission (including knot E; Fig. 5 frames 5 & 6) extending approximately north–south roughly *perpendicular* to the radio source axis. Part of this blueshifted region was detected in the spectroscopic observations of VM05.

3.2.2 EELR kinematics

Fig. 6 presents a quantified view of the [OIII]5007Å emission line data (flux, line width and velocity) for PKS1932-46 obtained via single Gaussian plus continuum fitting. The material lying to the west of the host galaxy displays the narrowest line widths, typically with measured FWHM of $\sim$ 200km s^{-1}(all line widths are corrected for instrumental broadening). The largest line widths (up to $\sim 300 - 750\mathrm{km\,s^{-1}}$) are observed towards the centre of the host galaxy, consistent with the line widths observed for [OIII] observed in VM98 and VM05. However, given the complex kinematics observed in these regions, single Gaussian fits to the line profile do not necessarily provide the most reliable measure of the true emission line FWHM.

In terms of the relative velocities of the different emission features, the knots in the western lobe are distinctly redshifted relative to the systemic velocity of the system, as can also be observed in Fig. 5. The line emission from the northern knot (labelled D in Figs. 4 and 5) is quite different; as the velocity map illustrates, there appears to be a fairly smooth velocity gradient of up to $\sim 400\mathrm{km\,s^{-1}}$ across this feature, with the material lying closest to the host galaxy emitting at shorter wavelengths than the more distant material. Similar variations are observed across the central regions of the EELR, as expected from the superposition of the structures observed in Fig. 5.

In order to analyse our IFU spectra at a higher signal–to–noise level and address the issue of superposed velocity structures, we have extracted and combined the spectra of fibres covering specific emission regions, and those which display similar kinematic properties. The resulting regions, labelled A to J, are displayed in Fig. 7. It should be noted that regions D and E on Fig. 7 cover feature D in figures 4 and 5, while region I (and to a lesser extent, J) on Fig. 7 corresponds most closely to feature E in figures 4 and 5. We have re-analysed the [OIII]5007Å line widths and velocity shifts, fitting up to three Gaussians to the combined emission line data. The results of our kinematic analysis are consistent between different lines, the earlier spectroscopy of VM98,

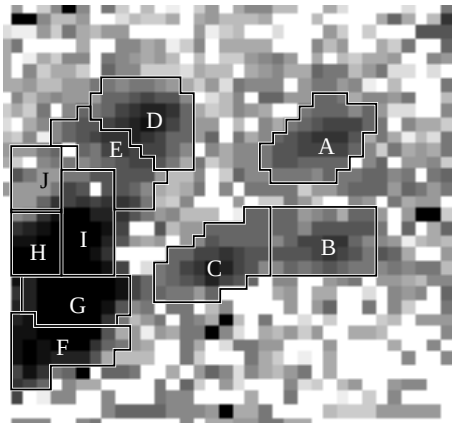

Figure 7. [OIII] flux image illustrating the ten multi-fibre regions extracted as part of our analysis of weaker emission lines. In the outer parts of the EELR, each region reflects an individual emission feature. In the central regions, we have selected fibres according to similar kinematic properties. The field of view of this image is approximately 23.5 × 23.5 arcsec squared.

and with the single-fibre data displayed in Fig. 6; we tabulate the results for [OIII]4959,5007 in Table 3.

In general, multiple Gaussian line profiles do not provide a better fit to the data than single Gaussian models. Most of the extended emission line regions appear to have relatively quiescent kinematics, i.e. small line widths and velocity shifts. The exceptions to this are regions G and I (see Fig. 8), where models combining multiple emission line components are more plausible. In these regions closer to the galaxy nucleus, the gas kinematics are more complex, and there are at least two clear velocity components (see Fig. 5): (i) the blue-shifted emission which lies in a north-south direction across regions I, G, F, and (ii) the "arm" feature (VM98) projecting eastwards from regions G & I at roughly the systemic redshift. Unfortunately, as is often the case for emission line fitting, there is some degeneracy between fits with two or more narrow components, and those combining both narrow and broader emission features. In addition to fits combining two narrow components, the preferred models for both the two- and three-component fits of region G also include a broader emission component (FWHM $\sim$ 1000 − 1200km s^{-1}; also observed in VM05), which is blueshifted relative to the systemic redshift by $\sim$ 200-500km s^{-1}.

3.2.3 EELR ionisation

Emission line ratio diagnostic diagrams provide a useful means of linking the observed line strengths to different ionisation mechanisms and ionising sources. The [OIII]/Hβ versus [NII]/Hα line ratio diagram (Baldwin, Phillips & Terlevich 1981) is one of the earliest and most popular diagrams of this sort, and can clearly distinguish between photoionised line emission from star forming galaxies, LINER galaxies and Seyferts/AGN. However, it should be noted that the use of a single line ratio diagram is inherently dangerous; the position of observational data relative to the predictions of different models does not always remain consistent between one diagram and another involving different emission line pairs (e.g. Inskip et al 2002b). These caveats aside, this diagram can still be used to shed light on the nature of the varied EELR components in our data.

While our data at observed-frame wavelengths shorter than 7200Å (including the [OIII]4959,5007Å, [OIII]4363Å and Hβ emission lines) are very clean, at longer wavelengths the data can be greatly affected by CCD fringing and the presence of bright sky lines (as was explained in some depth in section 2.1), and thus are subject to larger uncertainties in their relative fluxes. In the case of our second IFU data cube (which subtracts the flux from one pointing from the alternative pointing) the fibres for several regions of interest (i.e. regions D, E and J) contain object flux in *both* pointings. We therefore use the first data cube to determine the [NII]/Hα line ratios in these regions. As this alternative data cube is imperfectly corrected for fringing, the errors on this line ratio are noticeably larger for these regions.

Fig. 9 displays the [OIII]5007/Hβ vs. [NII]6583/Hα line ratio diagram for our IFS data. The observed line ratios are generally consistent with AGN photoionisation for the regions F, G and H. The western knots (A, C) and regions I and J exist in a noticeably different ionisation state, between the predictions of AGN photoionisation and the shock models with a photoionising precursor. Some interaction with the radio source may be plausible in the case of region C, although the quiescent kinematics in this region would argue against the presence of significant direct shock ionisation. Although the more varied kinematics observed in the central regions (F, G, H, I) might be suggestive of shocks, the line ratios for these regions do not place them significantly closer to the predictions of shock models except in the case of region I. The [NII]/Hα ratios of the blueshifted gas components (D, E) are also relatively low. Region D lies at a significant offset from the predictions of simple AGN photoionisation (dot-dashed track) which are compatible with regions G, H and F, but is well explained by AGN photoionisation including the presence of dust (dashed track). Region E is quite close to the maximum starburst track of Kewley et al (2001) on Fig. 9, and at a significant offset from the predictions of simple AGN photoionisation. Based on the emission line imaging of VM98, these regions are noticeably bright in [OII]3727Å emission, also indicating a fairly low ionisation state. It is most likely that the emission from these regions can be interpreted as being due to stellar photoionisation. This is consistent with the spectroscopic observations of VM05 (obtained using a slit PA of -5°, i.e. coincident with region E and the eastern side of region D), which identified a number of star forming regions in this part of the EELR.

3.3 Spitzer MIPS imaging, and the z=0.229 companion galaxy

It has been speculated in the past (VM98) that the galaxy lying to the north of PKS1932-46 could lie at a similar redshift. Previous imaging of this source suggested the possible presence of spiral arms, on the basis of the bright emission feature to the south-east, and the low surface brightness structure extending to the north-west. Our K_S-band imaging data (Figs. 2 and 10) represents a significant improvement in resolution and signal-to-noise, and clearly shows that this galaxy has a far more complicated morphology.

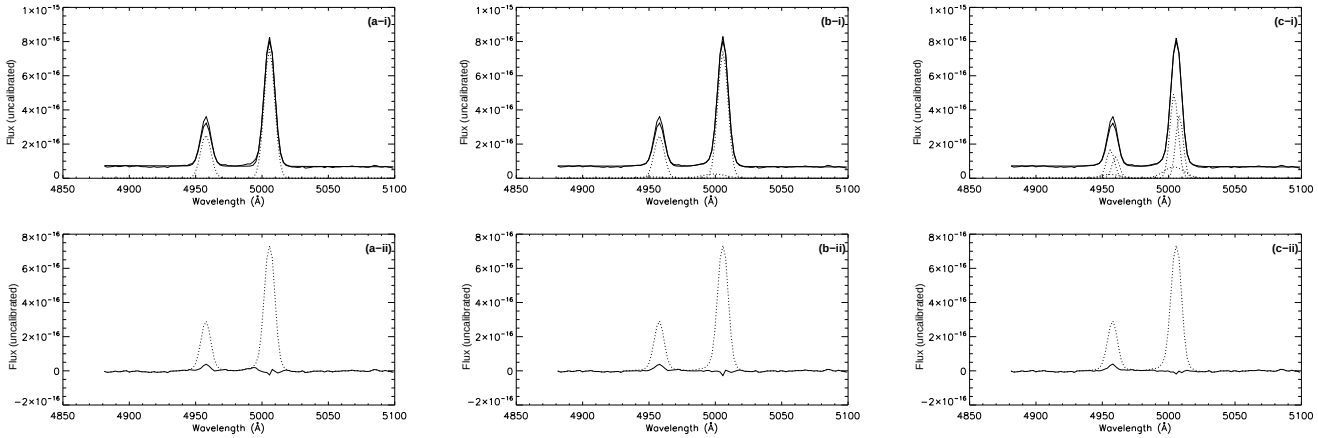

Figure 8. Comparison between fits of the O[III]5007Å emission from region G using different numbers of Gaussian components: a single Gaussian (a - left), two Gaussians (b - centre) and three Gaussians (c - right). In the top row (a-i, b-i, c-i), we display the observational data and the model fit (solid lines) together with the individual Gaussian components (dotted line). On the bottom row (a-ii, b-ii, c-ii), we display the observational data (dotted line) and the residuals after model subtraction (solid line).

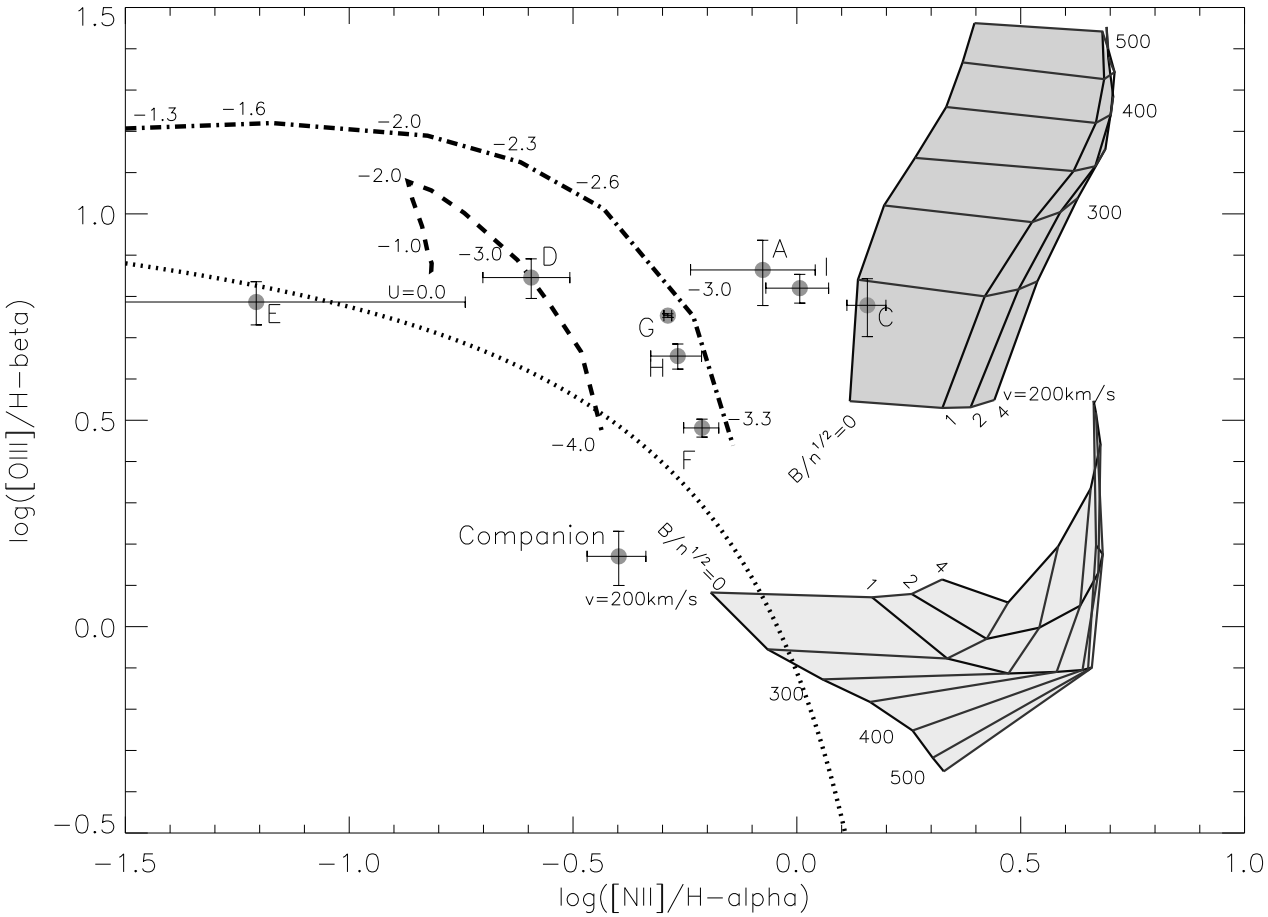

Figure 9. [OIII]/Hβ vs. [NII]/Hα emission line diagnostic diagram. The dotted line is the maximum starburst track of Kewley et al (2001). We also display the predictions of AGN photoionisation models (Groves, Dopita & Sutherland 2004) both excluding and including the effects of dust (dot-dashed and dashed lines respectively) for an electron density of $n_e = 100\mathrm{cm}^{-3}$ and a range of ionisation parameters ($0.0 > \log_{10}U > -4.0$). The grey regions represent the predictions of the shock models of Dopita & Sutherland (1996), with (dark grey) and without (light grey) a photoionising precursor region. The data points are for the regions illustrated in Fig. 7; regions B and J are absent due to large uncertainties, particularly on the [NII] emission line strength.

Table 3. Kinematics of the multi-fibre regions illustrated in Fig. 7. Velocity shifts are relative to the typical value of $z = 0.231$. Except for regions G and I (where 2 and 3 Gaussian fits are also presented), only a single Gaussian component is required for each region.

Region	Line Width (FWHM) ($km\,s^{-1}$)	Velocity Shift ($km\,s^{-1}$)	Reduced χ^2
A	189 ± 20	$+181 \pm 34$	1.40
B	198 ± 130	$+203 \pm 47$	1.50
C	215 ± 21	$+261 \pm 35$	0.90
D	229 ± 9	$+51 \pm 34$	1.27
E	153 ± 22	-65 ± 34	1.08
F	345 ± 15	-319 ± 35	1.09
G (single)	440 ± 2	-82 ± 34	2.10
G (double)	$442 \pm 2, 1208 \pm 118$	$-77 \pm 34,\ -480 \pm 66$	2.02
G (triple)	$179 \pm 7, 302 \pm 3, 1067 \pm 43$	$+87 \pm 34,\ -151 \pm 34,\ -189 \pm 40$	1.67
H	322 ± 15	$+87 \pm 34$	1.07
I (single)	417 ± 9	-134 ± 34	1.22
I (double)	$280 \pm 15, 512 \pm 20$	$-190 \pm 34,\ -37 \pm 35$	1.00
J	148 ± 178	$+95 \pm 49$	1.10

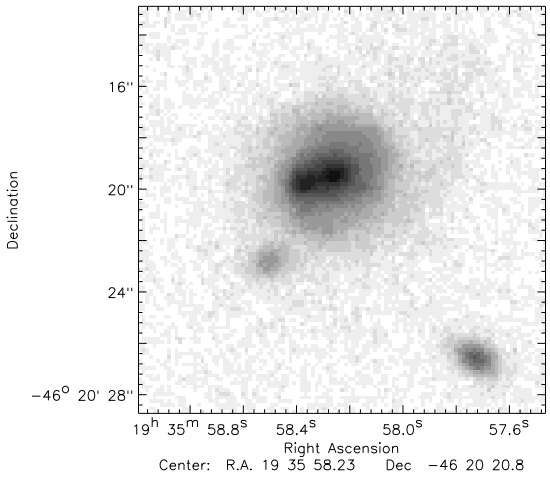

Figure 10. K_S-band image of the companion galaxy, revealing several very interesting morphological features: a double nucleus, tidal tail (extending northwards from the west ofthe galaxy; see also Fig 2), and several spatially resolved objects which may possibly be dwarf satellites.

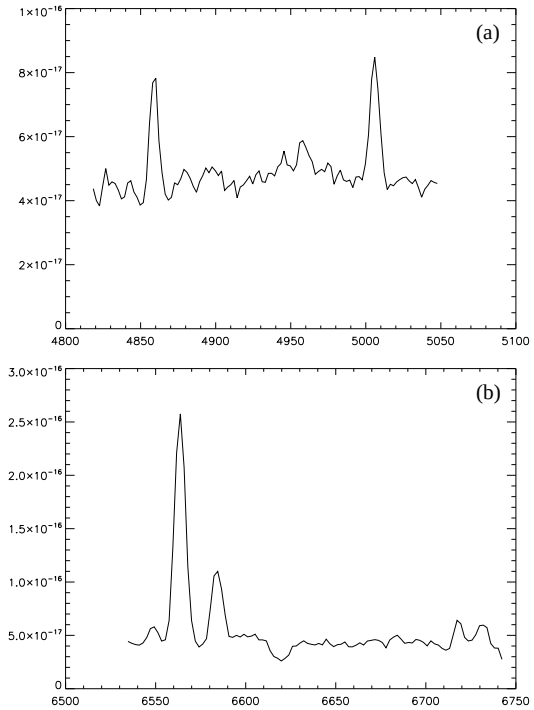

Figure 11. Spectra of the merging companion galaxy, illustrating the relative strengths of major emission lines (arbirtrtary flux units). (a - top) - the Hβ and [OIII]4959,5007Å emission lines. (b - bottom) - [NII]6549Å, Hα, [NII]6583Å and the [SII]6717,6734Å doublet.

Figure 10 displays the K_S-band image of this galaxy after adjusting the contrast levels. The north-west feature has the appearance of a tidal tail rather than a spiral arm, and the south-east emission feature is revealed as a separate object. More interestingly, the galaxy itself has a very distinctive double nucleus; this galaxy is almost certainly a merging system of some description.

Our IFS data include flux from the western edge of this galaxy, and confirm that it lies at a very similar redshift ($z = 0.2298 \pm 0.0002$) to PKS1932-46 itself ($z = 0.2307 \pm 0.0002$), i.e. with a rest-frame velocity shift of $\sim 220 \pm 70 \mathrm{km\,s^{-1}}$ between the two sources. There are some indications of a velocity gradient across the galaxy, but the narrow [OIII]5007 line widths typically suggest rather quiescent gas. Extracted spectra for this galaxy are displayed in Figure 11, illustrating the major emission lines: Hβ and the [OIII]5007 doublet, and also the [NII]6549,6583, Hα and [SII]6717,6734 lines at longer wavelengths. Using these data, we have plotted this galaxy on our BPT diagram (Fig. 9); the source clearly lies in the regime populated by star-forming galaxies.

In addition to very low [NII]/Hα line ratios in the companion galaxy spectra, Spitzer MIPS photometry of PKS1932-46 and its surrounds reveal that the companion galaxy is more luminous than the radio source at 24μm, and substantially more so at 70μm, also suggestive of vigorous star formation in the companion. These data are displayed in Fig. 12, and extracted aperture fluxes for both the radio galaxy and the companion galaxy are listed in table 2. On the basis of the measured MIPS fluxes extrapolated to the standard IRAS wavebands and the standard formula presented in Sanders & Mirabel (1996), we derive infrared luminosities in our assumed cosmology for the radio source

and interacting companion of $L_{IR} \gtrsim 1.96 \times 10^{44}\mathrm{ergs}^{-1}$ ($\gtrsim 5.1 \times 10^{10}\mathrm{L}_{\odot}$) and $L_{IR} \gtrsim 5.0 \times 10^{44}\mathrm{ergs}^{-1}$ ($\gtrsim 1.3 \times 10^{11}\mathrm{L}_{\odot}$) respectively, placing the companion galaxy within the range of luminosities expected for LIRG-type galaxies (Sanders and Mirabel). In addition, the relatively cool MFIR colours are also consistent with a starburst scenario.

4 DISCUSSION

4.1 The nature of the host galaxy

Like most powerful radio sources, the host galaxy of PKS1932-464 is a massive elliptical. In conjunction with previous modelling of the host galaxy stellar continuum, our modelling of the host galaxy morphology has allowed us to determine its mass ($M \sim 1.7 - 3.2 \times 10^{11}\mathrm{M}_{\odot}$) and size ($r_{\mathrm{eff}} \sim 9$kpc), which are fairly modest for a galaxy of this type. The size of the host galaxy is comparable to the median size of 3C sources at similar redshifts (~ 10kpc at $z = 0.2$), although somewhat smaller than the statistical mean ($\sim 12-15$kpc; McLure et al 1999, Roche & Eales 2000, Inskip et al 2005). The scatter in the radio galaxy $K-z$ relation (e.g. Inskip et al 2002c) suggests that a source at a redshift of $z = 0.231$ would be expected to have a $K-$band magnitude within the range $\sim 13 - 15.5$ magnitudes (at these redshifts, the mean and median $K-$band magnitude is ~ 14); our measured K_S-band magnitude for PKS1932-46 ($K_S = 15.3$) places it towards the fainter end of this range. Finally, assuming that there is little intrinsic mass/size variation between galaxies at redshifts of 0.2 to 0.7 (Inskip, Best and Longair 2006), the derived mass for PKS1932-46 lies towards the lower end of the range estimated for 3C galaxies ($\sim 1.5 - 6.5 \times 10^{11}\mathrm{M}_{\odot}$ in our assumed cosmology; Best et al 1998). We therefore conclude that the central super-massive black hole is also likely to be proportionately smaller than the mean value for radio galaxies of similar redshift.

4.2 The nature of the active nucleus

In terms of interpreting the nature of the AGN itself, it is productive to combine the results of different observational studies.

Spitzer MIPS photometry of a complete sample of 2Jy sources (Tadhunter et al 2007) has been used to address the issue of the dominant dust heating mechanism in AGN. The [OIII]5007Å emission line luminosity (which can be used as a tracer of AGN power, e.g. Rawlings & Saunders 1991; Tadhunter et al 1998; Simpson 1998) is strongly correlated with the mid-IR emission (Fig. 13), indicating that AGN illumination is the principal dust-heating mechanism.

It is notable that PKS1932-46 lies well below the least-squares fit to the data on the plot of $24\mu m$ vs. [OIII] luminosities (Fig. 13), and also at the lower end of the scatter of points of similar [OIII] luminosity. This can be interpreted in one of two ways: either (i) the AGN component of the dust heating is substantially weaker than might be expected for a source of that [OIII]5007Å emission line luminosity, or (ii) the source is overluminous in [OIII]5007Å emission. However, the latter explanation seems unlikely given that this object falls well within the scatter of the main correlation between [OIII] luminosity and radio power presented by Tadhunter et al (1998) (and is in fact close to the mean for sources of similar extended radio power).

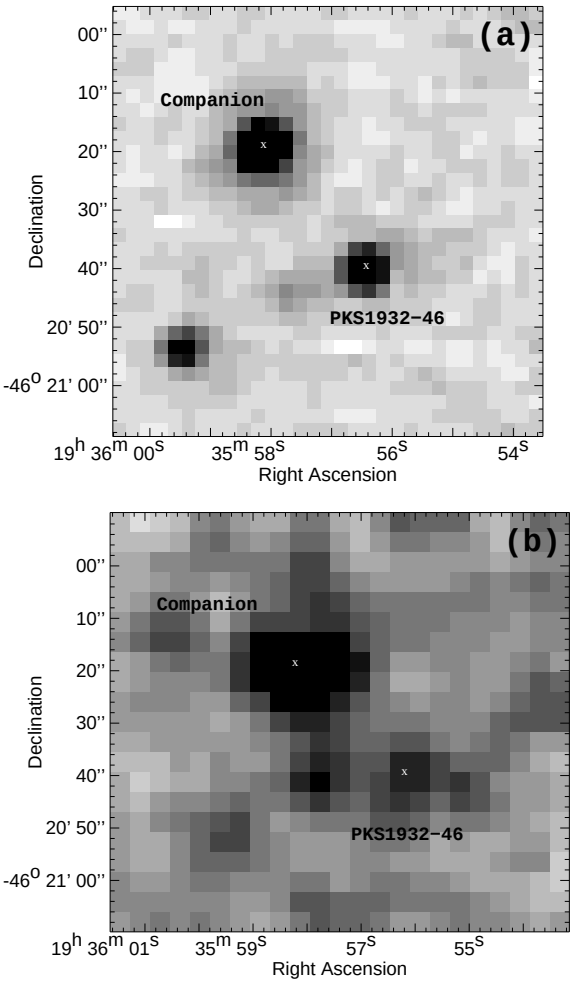

Figure 12. 24μm (a - top) and 70μm (b - bottom) Spitzer MIPS images of PKS1932-46 and surrounding objects. The pixel scales are 2.54 arcsec per pixel and 4 arscec per pixel for the 24μm and 70μm data respectively. The PSF FWHM is 6 arcsec for the 24μm data, and 18 arcsec for the 70μm data.

Observations at other wavelengths can help us to determine whether the active nucleus is genuinely underluminous. Long-slit spectroscopic observations of this source (Holt et al 2007) have identified a broad emission component in the Hα line, with $L_{H\alpha} \approx 1 \times 10^{41}\mathrm{ergs}^{-1}$. This broad component is significantly weaker than that detected in the spectra of other BLRGs in the 2Jy sample or low redshift 3C BLRGs (typically $5 \times 10^{42}\mathrm{ergs}^{-1}$ to several $10^{44}\mathrm{ergs}^{-1}$ in our assumed cosmology; Osterbrock, Koski & Phillips 1976). Using the equations of Greene and Ho (2005) relating $H\alpha$ luminosity and FWHM to black hole mass, the observed broad $H\alpha$ properties suggest a virial mass of $M_{BH} \sim 1.7 \times 10^{7}\mathrm{M}_{\odot} \pm 25\%$. However, based on our derived bulge mass for PKS1932-46, we would expect the central SMBH to have a substantially larger mass of 2 to $7.5 \times 10^{8}\mathrm{M}_{\odot}$ (McLure & Dunlop 2001, Marconi & Hunt 2003), appropriate for an $\sim L\star$ galaxy. This discrepancy suggests that either the central quasar itself is underluminous,

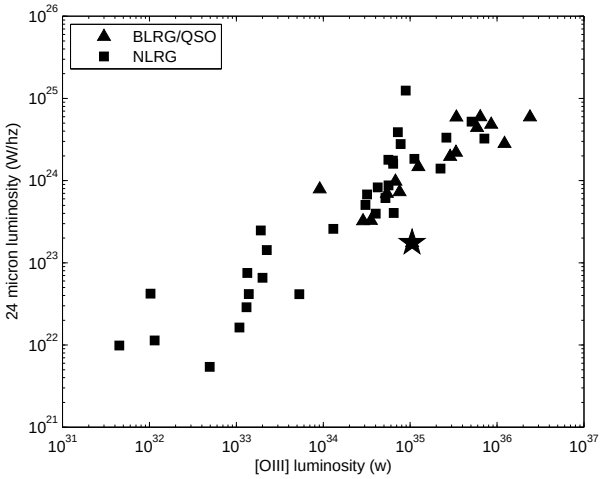

Figure 13. Reproduction of Figure 1 from Tadhunter et al (2007). Square and triangular symbols represent narrow-line radio galaxies (NLRGs) and quasars/broad-line radio galaxies (BLRGs) respectively, and PKS1932-46 is marked as a star.

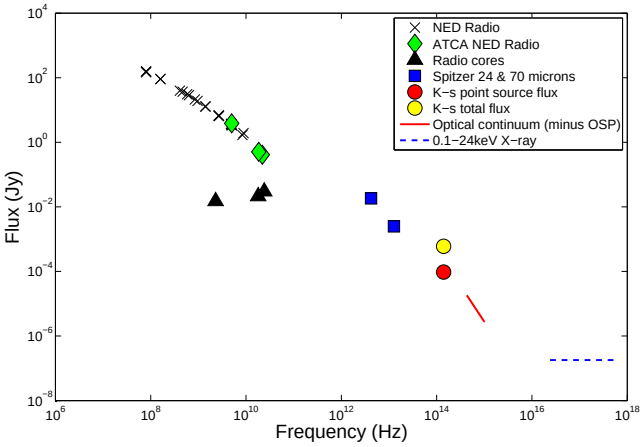

Figure 14. Spectral energy distribution for PKS1932-46. Radio data points are from NED and ATCA observations. The optical continuum is the best-fitting power-law contribution to the galaxy continuum emission after deduction of the old stellar population (Holt et al 2007). The X-ray data is for the average X-ray flux measured by Siebert et al (1996). Other data points are as presented in this paper.

or that a significant fraction of the broad emission is blocked from view.

At X-ray wavelengths, ROSAT X-ray observations of PKS1932-46 (Siebert et al 1996) showed that this source has an X-ray luminosity at 0.1-2.4keV of 6×10^{43}erg s^{-1} (assuming $H_0 = 50$km s^{-1}Mpc^{-1} and $q_0 = 0.0$), which corresponds to a luminosity of 3.3×10^{43}erg s^{-1} in our chosen cosmological model. This value is below the median average (4.6×10^{43}ergs^{-1}) for FRII BLRGs (Siebert et al 1996; see also Fabbiano et al 1984, Sambruna et al 1999). Although the X-ray emission is likely to be predominantly due to the AGN, the presence of a hot x-ray emitting halo associated with the host galaxy or a group/cluster environment can also contribute to the observed X-ray fluxes at some level. The observed X-ray luminosities (corrected for absorption) therefore represent upper-limits on the total X-ray emission from the AGN.

We can also consider these multi-wavelength data as a whole. Fig. 14 displays the observed-frame SED for PKS1932-46, from radio through to X-ray frequencies. In their modelling of radio source host galaxy stellar populations for PKS1932-46, Holt et al (2007) identified the presence of a power law component of the form $F_\nu \propto \nu^{-\alpha}$ with $\alpha = 2.23$ alongside the continuum emission from the old stellar population. There is some uncertainty in the slope of the optical power-law; although the continuum modelling of Holt et al (2007) is consistent with a combination of old stellar population and power law components, the addition of younger stellar populations and various degrees of reddening to the modelling leads to a range of acceptable power-law fits with spectral indices of $\alpha \gtrsim 1.4$ (c.f. $\alpha = 2.23$ for old stellar population models only) and reddening of the stellar populations of $0 < E(B-V) < 0.8$. Assuming that the AGN is responsible for the bulk of the 24μm emission and the 16% nuclear point source contribution in the K-band, the modelled IR–optical AGN contribution is a power-law with $\alpha = 1.4 \pm 0.15$, similar to the minimum modelled optical spectral index. This SED slope is redder than those measured for low redshift quasars (Simpson and Rawlings 2000), but certainly bluer than heavily extinguished objects such as 3C41 (Simpson and Rawlings 2000) and PKS1549-79 (Holt et al 2006).

In addition to the evidence obtained at other wavelengths, the broad Hα emission detected by VM98 and Holt et al (2007) is also weak. Taken together, these results all suggest that PKS1932-46 is powered by an underluminous AGN when compared with similar 2Jy sources. Interestingly, while the AGN appears to be underluminous at many wavelengths, the source remains powerful in terms of its narrow line emission from the nuclear regions. One means of explaining the discrepancy between the observed [OIII] and 24μm luminosities is in terms of the source geometry. If the bulk of the 24μm emission originates from the torus surrounding the active nucleus, a smaller than average covering factor for the torus relative to the NLR would lead to lower than expected 24μm emission. However, this would not explain the underluminous emission at X-ray and optical wavelengths. Most plausibly, AGN variability over timescales of $\lesssim 10^4$ years could account for the lower than average nuclear luminosities at all wavelengths. Given the differences in light travel times for the torus and NLR, it is plausible that the central quasar is currently in a lower state of activity, whereas the luminous [OIII] and radio emission reflect an epoch in the recent past when the AGN was more active.

Overall, we conclude that the AGN within PKS1932-46 is most likely to be powered by an AGN that is currently significantly less luminous than the AGN in most other sources in the wider 2Jy sample of similar redshift, and that it is likely that the power-output of the AGN has recently decreased.

4.3 EELR properties

The EELR of PKS1932-46 displays a diverse variety of features. In brief:

(i) The extended ionised structures display a variety of

ionisation mechanisms, with evidence for ionisation by the AGN, young stars and possibly also shocks with photoionising precursor regions. AGN photoionisation has a more obvious impact on the regions along or close to the radio structures, and in the vicinity of the AGN, while stellar ionisation becomes more significant at greater distances from the AGN ionisation cone.

(ii) Line emission is produced over a wide range of velocities across the EELR (redshifted by $\sim 200 - 300 \mathrm{km\,s^{-1}}$ in the western radio lobe, and blueshifted by a similar amount for the star forming material extending northwards from the host galaxy). However, the narrow line widths generally reflect fairly quiescent gas kinematics. Close to the host galaxy (i.e. within a projected distance of $\sim$ 20kpc from the AGN), the system displays multiple velocity structures along the line of sight. The broadest line widths (up to $\sim 1000 \mathrm{km\,s^{-1}}$) are also observed in this region.

The *lack* of disturbed kinematics in the outer regions of the EELR of PKS1932-46 is one of the noteworthy features of this source. Given that this source displays very little clear-cut evidence for shocks in the regions probed by our IFS data, the large extent of the kinematically quiescent material in the outer regions of the EELR is somewhat anomalous. Overall, the emission properties at large distances from the AGN are more typical of the photoionised material observed in less extensive low-redshift EELRs (Inskip et al 2002b), but also reminiscent of the kinematically quiescent material in the extensive gaseous haloes observed at high redshift (e.g. Reuland et al 2007). Understanding how this complex system came into being may shed light on the formation of higher redshift EELRs, and the causes of the observed evolution in their properties. In their spectroscopic study of the PA -9° material, VM05 suggested that the best explanation for the properties of this EELR was a series of compact, star-forming objects associated with the tidal debris of a merging system. Indeed, the narrowness of the observed emission lines is consistent with those measured in star-forming objects. We concur with this explanation for the various knots extending across north/south, which appear to form a large-scale linear structure in the foreground of the host galaxy.

However, for the quiescent material in the western radio lobe (which does not display signs of star formation) it may be less likely that the emitting material is self-gravitating. Assuming simple clouds of approximately 10pc in size, the material would be expected to dissipate over a relatively short timescale ($\sim 10^4$ years; e.g. Fabian et al 1987), placing the persistence of the EELR in question. While pressure-equilibrium with the hot-phase IGM in the galaxy halo could act as a confinement mechanism in this scenario, alternative descriptions of EELR clouds allow for longer lifetimes for the emitting regions, e.g. the overpressured mixed-medium clouds described by Robinson et al (2002).

Overall, a tidal or outflow origin for the EELR material (possibly associated with recent star formation) is a very plausible means of explaining its extreme size.

4.4 The local environment - an interacting group?

Redshift evolution is observed in a great many different aspects of the EELRs associated with powerful radio galaxies, and in many ways PKS1932-46 bears more resemblance to high-redshift systems than its low redshift counterparts. It is plausible that the similarities between the properties of PKS1932-46 and higher redshift systems could be explained by the nature of its local environment.

Our K_S-band imaging of PKS1932-46 reveals a large number of faint features in the surrounding field, as well as several bright objects. The large galaxy to the northeast of PKS1932-46 is clearly a very disturbed system, displaying multiple nuclei, tidal tails and evidence for significant ongoing star formation. This companion galaxy lies at an identical redshift to the star-forming material extending north-south across PKS1932-46. However, the richest cluster environments are ruled out by the observed X-ray luminosity of PKS1932-46, which does not allow for a strong contribution to the X-ray emission from a hot IGM.

We suggest that PKS1932-46 is a member of an interacting galaxy group, and that a large proportion of the EELR material may originate from the tidal debris of previous interactions (plausibly ejected giant molecular clouds in the case of the star forming regions), either between PKS1932-46 and the companion galaxy, or from a previous merger event. Such events, likely to be more common at higher redshifts, may plausibly also have been responsible for triggering the current radio source activity (e.g. Heckman et al 1986, Wilson & Colbert 1995), and can almost certainly explain why this source displays such dramatic features in its EELR. It is interesting to note that although starbursts and AGN activity may represent two major manifestations of mergers and interactions (e.g. Springel et al 2005), they are separated within this group: nuclear activity is dominant in the radio galaxy PKS1932-46, whereas the dominant star formation activity in this group is associated with the companion galaxy.

The nature of the surrounding environment also has implications for our interpretation of the observed galaxy and EELR properties; specifically, increasing the filling factor of line-emitting clouds can have several knock-on effects for a source such as this. A source with a specific AGN/jet power would be observed to have a larger radio luminosity when existing in a higher-density environment (e.g. Kaiser, Dennett-Thorpe & Alexander, 1997) than it would otherwise. Further, boosting of the observed [OIII] line emission due to other processes would mean that the measured line luminosity would no longer be indicative of the intrinsic AGN/jet power of the source. It is plausible that both of these factors are at work in the case of PKS1932-46, and that this may also be the cause of its departure from the correlation between the [OIII] and mid- to far-IR luminosities in the 2Jy sample.

5 CONCLUSIONS

Our multiwavelength observations of PKS1932-46 have led to the following results:

- The host galaxy is an $\sim M_\star$ elliptical containing a moderately powerful AGN. Although weak broad line emission has been observed from this source, the AGN luminosity is likely to be relatively low for a source of this radio power. The observed BLRG features suggest that any obscuration of the nuclear regions is moderate at best, and that the

AGN is intrinsically weaker than average for the sample, and thus not all powerful FRII radio sources are associated with highly luminous quasar nuclei. Further, it is probable that the power-output of the AGN has dropped significantly over the past 10^4 years.

• The extensive emission line region surrounding this galaxy consists of kinematically quiescent, AGN-photoionised material within the radio lobe, and a band of star-forming knots extending north-south, lying perpendicular to the radio axis and offset by velocities of a few hundred $\mathrm{km\,s^{-1}}$. We observe evidence for a gradient in the EELR ionisation mechanism, such as that observed in higher redshift sources.

• PKS1932-46 lies in a group environment, which is dominated by the merging galaxy to the north east. Unusually it is this companion object, rather than the radio source host galaxy, which is undergoing the bulk of the star formation activity within the group. However, it is likely that past/ongoing interactions within the group may be responsible for both the triggering of the radio source, and also the richness of the spectacular EELR.

ACKNOWLEDGMENTS

KJI acknowledges support from a PPARC research fellowship, JH a PPARC PDRA, and DD a PPARC research studentship. The work of MV-M has been supported by the Spanish Ministerio de Educación y Ciencia and the Junta de Andalucía through the grants AYA2004-02703 and TIC-114. This work is based in part on observations made with the Spitzer Space Telescope, which is operated by the Jet Propulsion Laboratory, California Institute of Technology under a contract with NASA. The IFS data published in this paper have been reduced using VIPGI, designed by the VIRMOS Consortium and developed by INAF Milano; KJI would particularly like to thank Paolo Franzetti for guidance in the use and reliability of the VIPGI software. We also thank the ESO technical and support staff for indulging our request for the use of SOFI in the small field mode. This research has made use of the NASA/IPAC Extragalactic Database (NED) which is operated by the Jet Propulsion Laboratory, California Institute of Technology, under contract with the National Aeronautics and Space Administration. We thank the referee, Alan Stockton, for his careful consideration of the manuscript.

REFERENCES

Allen M. G., et al, 2002, ApJS, 139, 411
Baldwin J. A., Phillips M. M., Terlevich R., 1981, PASP, 93, 5
Best P. N., Röttgering H. J. A., Longair M. S., 2000, MNRAS, 311, 23
Best P. N., Longair M. S., Röttgering H. J. A., 1998, MNRAS, 295, 549
Bruzual G., Charlot S., 2003, MNRAS, 344, 1000
Chambers K. C., Miley G. K., van Breugel W. J. M., 1987, Nature, 329, 604
Dopita M. A., Sutherland R. S., 1996, ApJS, 102, 161
Dunlop J. S., McLure R. J., Kukula M. J., Baum S. A., O'Dea C. P., Hughes D. H., 2003, MNRAS, 340, 1095
Elvis M., et al, 1994, ApJS, 95, 1
Fabbiano G., Miller L., Trinchieri G., Longair M., Elvis M., 1984, ApJ, 277, 115
Fabian A. C., Crawford C. S., Johnstone R. M., Thomas P. A., 1987, MNRAS, 228, 963
Fu H., Stockton A., 2007, ApJ, in press, astro-ph/0705.4365
Gordon K., et al, 2005, PASP, 117, 503
Greene J. E., Ho L. C., 2005, ApJ, 630, 122
Groves B. A., Dopita M. A., Sutherland R. S., 2004a, ApJS, 153, 9
Groves B. A., Dopita M. A., Sutherland R. S., 2004b, ApJS, 153, 75
Heckman T. M., Smith E. P., Baum S. A., van Breugel W. J. M., Miley G. K., Illingworth G. D., Bothun G. D., Balick B., 1986, ApJ, 311, 526
Holt J., Tadhunter C. N., González Delgado R. M., Inskip K. J., Rodriguez J., Emonts B. H. C., Morganti R., Wills K. A., 2007, MNRAS, in press
Holt J., Tadhunter C. N., Morganti R., Bellamy M., González Delgado R. M., Tzioumis A., Inskip K. J., 2006, MNRAS, 370, 1633
Howarth I. D, 1983, MNRAS, 203, 301
Inskip K. J., Best P. N., Longair M. S., 2006, MNRAS, 367, 693
Inskip K. J., Best P. N., Longair M. S., Röttgering H. J. A., 2005, MNRAS, 359, 1393
Inskip K. J., Best P. N., Rawlings S., Longair M. S., Cotter G., Röttgering H. J. A., Eales S., 2002a, MNRAS, 337, 1381
Inskip K. J., Best P. N., Röttgering H. J. A., Rawlings S., Cotter G., Longair M. S., 2002b, MNRAS, 337, 1407
Inskip K. J., Best P. N., Longair M. S., MacKay D. J. C., 2002c, MNRAS, 329, 277
Jarvis M. J., Wilman R. J., Röttgering H. J. A., Binette L., 2003, MNRAS, 338, 263
Kaiser C. R., Dennett-Thorpe J., Alexander P., 1997, MNRAS, 292, 723
Kaspi S., Smith P. S., Netzer H., Maoz D., Jannuzi B. T., Giveon U., 2000, ApJ, 533, 631
Kewley L. J., Dopita M. A., Sutherland R. S., Heisler C. A., Trevena J., 2001, ApJ, 556, 121
Kochanek C. S., et al, 2001, ApJ, 560, 566
Le Févre O., et al, 2003, SPIE, 4841, 1670
Makovoz D., Marleau F. R., 2005, PASP, 117, 1113
Makovoz D., Khan I., 2005, in Shopbell P., Britton M., Ebert R., eds, ASP Conf. Ser. Vol. 347, Astronomical Data Analysis Software and Systems XIV, Astron. Soc. Pac., San Francisco, p81
Marconi A., Hunt L. K., 2003, ApJ, 589, L21
Masci F. J., Laher R., Fang F., Fowler J. W., Lee W., Stolovy S., Padgett D., Moshir M., 2005, in Shopbell P., Britton M., Ebert R., eds, ASP Conf. Ser. Vol. 347, Astronomical Data Analysis Software and Systems XIV, Astron. Soc. Pac., San Francisco, p468
McCarthy P. J., van Breugel W, Spinrad H, Djorgovski S., 1987, ApJ, 321, L29
McLure R. J., Dunlop J. S., 2001, MNRAS, 327, 199
McLure R. J., Kukula M. J., Dunlop J. S., Baum S. A., O'Dea C. P., Hughes D. H., 1999, MNRAS, 308, 377
Moorwood A., Cuby J. G., Lidman C. 1998, The Messenger, 91, 9
Morganti R., Oosterloo T. A., Reynolds J. E., Tadhunter C. N., Migenes V., 1997, MNRAS, 284, 541
Morganti R., Killeen N. E. B., Tadhunter C. N., 1993, MNRAS, 263, 1023
Moy & Rocca-Volmerange, 2002, A&A, 383, 46
Osterbrock D. E., Koski A. T., Phillips M. M., 1976, ApJ, 206, 898
Persson S. E., Murphy D. C., Krzeminski W., Roth M., Rieke M. J., 1998, AJ, 116, 2475
Rawlings S., Saunders R., 1991, Nat, 349, 138
Reuland M., et al, 2007, AJ, 133, 2607

Robinson T. G., Tadhunter C. N., Dyson J. E., 2002, MNRAS, 331, L13
Rieke G. H., et al, 2004, ApJS, 154, 25
Roche N., Eales S. A., 2000, MNRAS, 317, 120
Röttgering H. J. A., Hunstead R. W., Miley G. K., van Ojik R., Wieringa M. H., 1995, MNRAS, 277, 389
Sambruna R. M., Eracleous M., Mushotzky R. F., 1999, ApJ, 526, 60
Sanders D. B., Mirabel I. F., 1996, ARA&A, 34, 749
Schlegel D. J., Finkbeiner D. P., Davis M., 1998, ApJ, 500, 525
Scodeggio M., et al, 2005, PASP, 117, 1284
Sérsic J. L., 1968, Atlas de Galaxias Australes (Córdoba: Observatorio Astronomico)
Siebert J., Brinkmann W., Morganti R., Tadhunter C. N., Danziger I. J., Fosbury R. A. E., di Serego Alighieri S., 1996, MNRAS, 279, 1331
Simpson C., Rawlings S., 2000, MNRAS, 317, 1023
Simpson C., 1998, MNRAS, 297, L39
Solórzano-Iñarrea et al., 2002, MNRAS, 331, 673
Springel V., Di Matteo T., Hernquist L., 2005, MNRAS, 361, 776
Stockton A., MacKenty J. W., Hu E. M., Kim T.-S., 2002, ApJ, 572, 735
Stoughton C., et al, 2002, AJ, 123, 485
Tadhunter C. N., Villar-Martín, M., Morganti R., Bland-Hawthorn J., Axon, D., 2000, MNRAS, 314, 849
Tadhunter C., et al, 2007, ApJL, 661, L13
Tadhunter C. N., Marconi A., Axon D., Wills K., Robinson T. G., Jackson N., 2003, MNRAS, 342, 861
Tadhunter C. N., Morganti R., Robinson A., Dickson R., Villar-Martín M., Fosbury R. A. E., 1998, MNRAS, 298, 1035
Tadhunter C. N., Morganti R., di Serego Alighieri S., Fosbury R. A. E., Danziger I. J., 1993, MNRAS, 263, 999
van Ojik R., Röttgering H. J. A., Miley G. K., Hunstead R. W., 1997, A&A, 317, 358
Villar-Martín M., Tadhunter C., Morganti R., Holt J., 2005, MNRAS, 359, L5 (VM05)
Villar-Martín M., Vernet J., di Serego Alighieri S., Fosbury R., Humphrey A., Pentericci L., 2003, MNRAS, 346, 273
Villar-Martín M., Tadhunter C., Morganti R., Clark N., Killeen N., Axon D., 1998, A&A, 332, 479 (VM98)
Willott C. J., Rawlings S., Jarvis M. J., Blundell K. M., 2003, MNRAS, 339, 173
Werner M., et al, 2004, ApJS, 154, 1
Wilson A. S., Colbert E. J. M., 1995, ApJ, 438, 62
Zanichelli A., et al, 2005, PASP, 117, 1271